Chinese Chemical Letters 36 (2025) 109989

Contents lists available at ScienceDirect

Chinese Chemical Letters

journal homepage: www.elsevier.com/locate/cclet

Noble metal clusters substitution in porous Ni substrate renders high mass-specific activities toward oxygen evolution reaction and methanol oxidation reaction

Fenglin Wang[a], Chengwei Kuang[a], Zhicheng Zheng[a], Dan Wu[a], Hao Wan[b], Gen Chen[a,*], Ning Zhang[a], Xiaohe Liu[b,*], Renzhi Ma[c,*]

[a] School of Materials Science and Engineering, Key Laboratory of Electronic Packaging and Advanced Functional Materials of Hunan Province, Central South University, Changsha 410083, China
[b] Zhongyuan Critical Metals Laboratory, Zhengzhou University, Zhengzhou 450001, China
[c] Research Center for Materials Nanoarchitectonics (MANA), National Institute for Materials Science (NIMS), Tsukuba, Ibaraki 305-0044, Japan

ARTICLE INFO

Article history:
Received 6 March 2024
Revised 9 April 2024
Accepted 9 May 2024
Available online 11 May 2024

Keywords:
Size effect
Pd cluster
Mass activity
Oxygen evolution reaction
Methanol oxidation reaction

ABSTRACT

The sluggish reaction kinetics of the oxygen evolution reaction (OER) and methanol oxidation reaction (MOR) remain obstacles to the commercial promotion of water splitting and direct methanol fuel cells. Considering the vital role of noble metals in electrocatalytic activity, this work focuses on the rational synthesis of Ni-noble metal composite nanocatalysts for overcoming the drawbacks of high cost and susceptible oxidized surfaces of noble metals. The inherent catalytic activity is improved by the altered electronic structure and effective active sites of the catalyst induced by the size effect of noble metal clusters. In particular, a series of Ni-noble metal nanocomposites are successfully synthesized by partially introducing noble metal into Ni with porous interfacial defects derived from Ni-Al layered double hydroxide (LDH). The $Ni_{10}Pd_1$ nanocomposite exhibits high OER catalytic activity with an overpotential of 0.279 V at 10 mA/cm^2, surpassing $Ni_{10}Ag_1$ and $Ni_{10}Au_1$ counterparts. Furthermore, the average diameter of Pd clusters gradually increases from 5.57 nm to 44.44 nm with the increased proportion of doped Pd, leading to the passivation of catalytic activity due to the exacerbated surface oxidation of Pd in the form of Pd^{2+}. After optimization, $Ni_{10}Pd_1$ delivers significantly enhanced OER and MOR electroactivities and long-term stability compared to that of Ni_2Pd_1, Ni_1Pd_1 and Ni_1Pd_2, which is conducive to the effective utilization of Pd and alleviation of surface oxidation.

Owing to the rapid consumption of conventional fossil fuels and global environmental pollution, the exploration of sustainable clean energy with low-cost is stimulated [1,2]. Water splitting has emerged as an efficient method for hydrogen generation [3-6], however, is generally limited by the sluggish kinetics of four-electron transfer OER for oxygen-oxygen double bonds [7-9]. Besides hydrogen energy, direct methanol fuel cells (DMFC), another appealing energy conversion technology due to the high energy density and reproducibility of methanol, is also seriously impeded by the sluggish MOR at anodic electrocatalysts [10-12]. Generally, electrocatalysts, the core assembly unit, play a crucial role in directly determining the catalytic performance of both OER and MOR. It is urgent to overcome the kinetic barrier by designing and synthesizing electrocatalysts for OER and MOR with high electroactivity and long-term stability.

Previous reports have revealed that noble metal-based composites (such as Ru, Ir, Pt and Pd) exhibited outstanding electroactivity due to their superior kinetics [13,14]. However, their large-scale and practical application is restricted by the high cost and relative scarcity of the noble metals [15-19]. Substantial efforts have been devoted to enhancing the catalytic activity efficiency as well as improving the atomic utilization of noble metal *via* precisely regulating chemical components, microstructures, and particle sizes [20,21]. In contrast, 3d transition metals (Ni, Co, Fe, *etc.*) have garnered increasing attention in catalysis and energy conversion/storage fields due to low cost and earth abundance [22,23]. Notably, Ni metal serves as an excellent electrocatalyst for promoting various reactions because of its variable valence states and phase transitions [24,25]. Nevertheless, the electrocatalytic performance of Ni metal is hindered by partial oxidation, inactivity and

* Corresponding authors.
E-mail addresses: geenchen@csu.edu.cn (G. Chen), liuxh@csu.edu.cn (X. Liu), MA.Renzhi@nims.go.jp (R. Ma).

https://doi.org/10.1016/j.cclet.2024.109989
1001-8417/

lost conductivity during the electrochemical cycle, which significantly limits its effectiveness.

Based on the above considerations, numerous investigations emerge for the design and development of novel catalysts, aiming at improving the catalytic activities and noble metal utilization, such as manipulating the structures and chemical components through exposing the ideal crystallographic facets of catalysts, alloying and/or combining noble metals with 3d transition metals [26-29]. Recently, controlling particle size and morphology has also become a common approach to overcome the above obstacles, such as core@shell nano-octahedra [30], nanocages [31,32], hollow nanocubes [33]. Among these, the design of metallic clusters stands out as a more economical, simple and feasible strategy *via* directly loading noble metals onto substrates, such as the construction of Ni-noble metal catalysts [34,35]. The synergy of introducing a trace of noble metal and particle size effect facilitates the superior electrocatalytic activity due to the formation of abundant active sites, strong corrosion resistance and improved conductivity.

Herein, well-defined $Ni_{10}Pd_1$, $Ni_{10}Au_1$ and $Ni_{10}Ag_1$ nanoplates were prepared *via* the displacement reactions. The uniform dispersion of trace noble metals on Ni significantly influenced the OER activities in an alkaline. Particularly, $Ni_{10}Pd_1$ nanocomposite exhibited superior OER activity and long-term cycling to $Ni_{10}Au_1$ and $Ni_{10}Ag_1$. Additionally, Ni_2Pd_1, Ni_1Pd_1 and Ni_1Pd_2 were further synthesized by adjusting the Pd concentration to investigate the size effect of Pd metal clusters on both OER and MOR catalytic activity. The size of Pd clusters grew from 5.57 nm to 44.44 nm with increased Pd concentration, which severely exacerbated the oxidation of Pd surface in Pd^{2+}, thus reduced the efficacious metal active sites and weakened the catalytic performance. As a result, $Ni_{10}Pd_1$ exhibited not only higher OER mass activity of 0.085 A/mg_{Pd} at 1.50 V but also excellent MOR mass activity of about 0.401 A/mg_{Pd} at 0.71 V. This work proposed a facile strategy to prepare high-performance Ni-noble metal-based electrocatalysts by incorporating trace noble metals, which improved the noble metal utilization and the availability of active metal sites.

A series of Ni-noble metal nanoplates (Ni-Pd, Ni-Au and Ni-Ag) were prepared through the partial replacement of nanoplate-assembled flower-like Ni precursor which was derived from Ni-Al LDH counterpart (Fig. 1). In detail, Ni-Al LDH was prepared by an oil bath process using $NiCl_2{\cdot}6H_2O$, $AlCl_3{\cdot}6H_2O$, and urea as the raw materials. Subsequently, Ni nanoplates were successfully synthesized through successively treating Ni-Al LDH nanoplates with hydrazine hydrate and NaOH solution in another hydrothermal system. The preparation of Ni nanoplates from Ni-Al LDH precursor generated porous defects during the removal of Al element, which was conducive to loading noble metals. Ni-noble metal nanoplates ($Ni_{10}Pd_1$, $Ni_{10}Au_1$, $Ni_{10}Ag_1$, Ni_2Pd_1, Ni_1Pd_1 and Ni_1Pd_2) were acquired by partially displacing the Ni with noble metals through a displacement reaction.

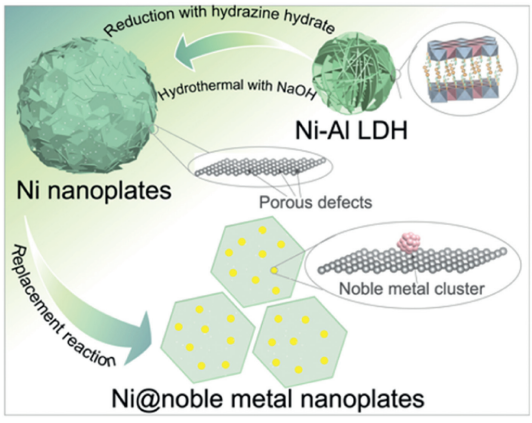

Fig. 1. Synthetic illustration of Ni-noble metal nanoplates.

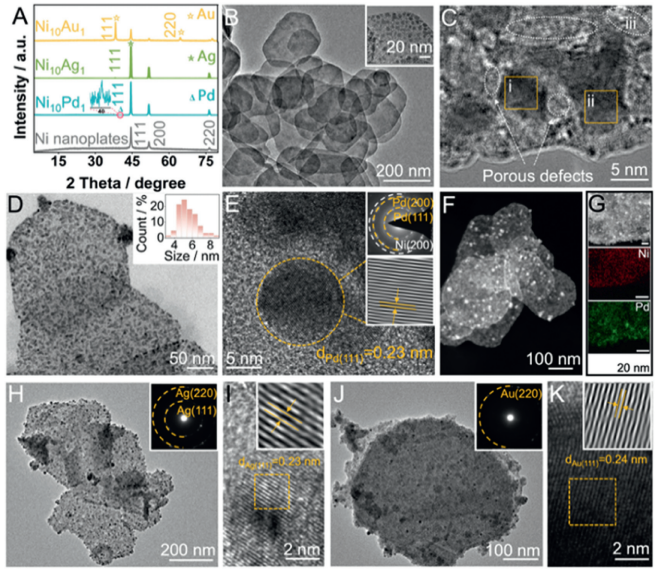

Fig. 2. Compositional and structural characterizations. (A) XRD patterns. (B) TEM and (C) HRTEM images of Ni nanoplates. (D) TEM and Pd particle size distribution of $Ni_{10}Pd_1$ nanoplates. (E) HRTEM image, (F) the HADDF-STEM and (G) the corresponding elemental mapping of $Ni_{10}Pd_1$ nanoplates. (H) TEM and SAED, (I) HRTEM of $Ni_{10}Ag_1$ nanoplates. (J) TEM and SAED, (J) HRTEM of $Ni_{10}Au_1$ nanoplates.

Fig. 2A and Fig. S1 (Supporting information) show the XRD patterns of as-prepared samples, from with high crystallinity of Ni-Al LDH product was detected [36]. The intermediate product after treating by hydrazine hydrate was composed by AlO(OH) (JCPDS No. 21−1307) and Ni (JCPDS No. 65−2865) (Fig. S2 in Supporting information). The pure metallic Ni was obtained by further treated with NaOH. The strong-diffraction peaks at 44.5°, 51.9° and 76.8° well matched with the (111), (200) and (220) reflections of cubic Ni phase, respectively. While for the XRD traces of the composites, the diffractions of Pd, Au or Ag metal were also detected, which proved the co-existence of Ni with the noble metals in the as-obtained composites. The hierarchical flower-like morphology assembled by hexagonal nanoplates of pure Ni is displayed in Fig. S3 (Supporting information), in good consistency with Ni-Al LDH (Fig. S4 in Supporting information). The representative TEM image of Ni nanoplates revealed the presence of numerous hexagonal nanoplates around 200 nm (Fig. 2B). The magnified TEM image, as in the inset in Fig. 2B, exhibited the formation of porous interfacial defects on the pure Ni nanoplates. The high-resolution electron microscope (HRTEM) image also distinctly illustrated the same phenomenon (Fig. 2C). The different regions of HRTEM were extracted by the inverse fast Fourier transformation (FFT) operation (Figs. S5, S6A and B in Supporting information). The lattice fringes with a plane spacing of 0.18 nm representing (111) crystal plane of cubic Ni were observed in regions i and ii. In addition, the numerous amorphous areas were also presented (region iii), representing the formation of porous interfacial defects after removing Al treatments. The selected area electron diffraction (SAED) pattern of hexagonal Ni nanoplates showed the diffraction rings of (111) and (220) planes of cubic Ni, confirming the polycrystalline nature (Fig. S6C in Supporting information). The nanoplate-like porous defect structures may enhance the efficiency of the subsequent displacement reaction and thus facilitate the effective reduction and adsorption of noble metal components on the surface of Ni nanoplates.

To further explore the deposition states of noble metals, comprehensive SEM and TEM analyses were conducted on Ni-noble

metal catalysts. The $Ni_{10}Pd_1$ nanoplates substantially retained distinctive lamellar morphology, as illustrated in the representative SEM image in Fig. S7A (Supporting information). The corresponding EDS result demonstrated that the Ni to Pd ratio was close to 10:1, which is approximately the same as the ratio of input raw materials (Fig. S8 in Supporting information). Notably, numerous Pd clusters, uniformly distributed on the surfaces of hexagonal Ni nanoplates with an average particle size of 5.57 nm, were observed (Fig. 2D and Fig. S7B in Supporting information). The lattice fringes of particle clusters are measured as representing the Pd (111) crystal plane with a crystal plane spacing of 0.23 nm in HRTEM and corresponding inverse FFT images (Fig. 2E). The SAED pattern shows the diffraction rings of different crystallographic planes for Ni and Pd, confirming the simultaneous presence of Ni and Pd within the $Ni_{10}Pd_1$ nanoplates. The high-angle annular dark-field STEM (HADDF-STEM), as shown in Fig. 2F, demonstrated bright spots on the hexagonal nanoplates, corresponding to metal particles with larger atomic numbers, *i.e.*, Pd. The elemental mapping (Fig. S9 in Supporting information) exhibited the coexistence of Ni and Pd elementals, which fully confirmed that Pd has successfully replaced Ni in the process of displacement reaction. Furthermore, the HADDF-STEM image and elemental mapping of $Ni_{10}Pd_1$ nanoplates verified the uniform distribution of Ni and Pd throughout the nanoplate (Fig. 2G).

The morphologies of the obtained $Ni_{10}Ag_1$ and $Ni_{10}Au_1$ composites closely resembled the hexagonal nanoplates of the Ni substrate (Figs. S7C and D in Supporting information), indicating the robust stability of the Ni precursor structure derived from Ni-Al LDH during the displacement reaction. Additionally, the corresponding EDS result confirmed the presence of Ag and Au in the $Ni_{10}Ag_1$ and $Ni_{10}Au_1$ composites after the reaction, respectively (Figs. S10 and S11 in Supporting information). Fig. 2H and Fig. S12A (Supporting information) show the TEM image of $Ni_{10}Ag_1$ composite in which Ag clusters with an average particle size of 11.55 nm were anchored on the Ni nanoplates. The (111) and (220) diffraction rings of the Ag element are detected in the SAED pattern, as displayed in the inset of Fig. 2H, indicating the polycrystalline nature. The HRTEM and corresponding inverse FFT images of $Ni_{10}Ag_1$ revealed the lattice fringes of Ag (111) plane spacing of 0.23 nm (Fig. 2I and Fig. S13 in Supporting information). Similarly, the TEM image of $Ni_{10}Au_1$ nanoplates indicated that Au clusters (particle size of 10.47 nm) were also anchored on Ni substrate (Fig. 2J and Fig. S12B in Supporting information). The SAED pattern showed the diffraction ring of (220) face of the Au element. The HRTEM and inverse FFT images present the crystallographic structure of Au with (111) lattice spacing of 0.24 nm (Fig. 2K and Fig. S14 in Supporting information), which were consistent with the XRD results of $Ni_{10}Au_1$ nanoplates.

The electrocatalytic OER activity of as-prepared Ni-noble metal nanocomposites were evaluated in 1.0 mol/L KOH solution (Fig. 3A). The OER activity of $Ni_{10}Pd_1$ nanoplates is superior to that of $Ni_{10}Ag_1$ and $Ni_{10}Au_1$. According to our previously reported research, the pure Ni demonstrates a high overpotential of 0.4 V delivering a current density of 10 mA/cm^2 [36]. In contrast, the $Ni_{10}Pd_1$ nanoplates required a smaller overpotential of only 0.279 V while $Ni_{10}Ag_1$ and $Ni_{10}Au_1$ exhibited the 0.382 V and 0.373 V, respectively (Fig. 3B), outperformed reported similar materials (Table S1 in Supporting information). Moreover, $Ni_{10}Pd_1$ catalyst demonstrated a higher O_2 production rate of approximately 156.67×10^{14} cm^{-2} s^{-1} (Fig. 3C). The Tafel slope for $Ni_{10}Pd_1$ (68 mV/dec) is significantly lower than 158 mV/dec for $Ni_{10}Ag_1$ and for 134 mV/dec for $Ni_{10}Au_1$ (Fig. 3D). Additionally, $Ni_{10}Pd_1$ nanoplates also possessed high durability over 42 h at 10 mA/cm^2, indicating its practical applicability (Fig. 3E). Both the activity and durability of $Ni_{10}Pd_1$ nanoplates fully demonstrate the suitability of Pd over Ag and Au for enhancing the OER performance.

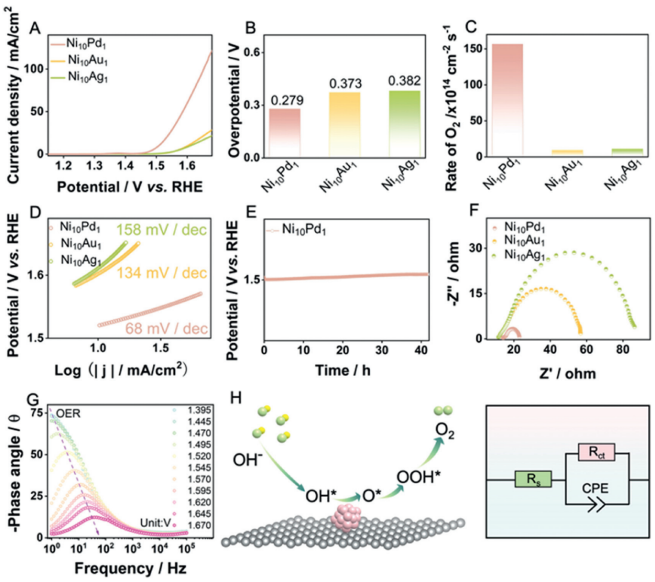

Fig. 3. OER measurements for Ni-noble metal composites. (A) IR-corrected LSV curves, (B) overpotential delivering 10 mA/cm^2, (C) production rate of O_2, (D) Tafel slopes. (E) chronoamperometry curves of $Ni_{10}Pd_1$ nanoplates at 10 mA/cm^2. (F) Nyquist plots of Ni-metal electrocatalysts. (G) Bode plots for $Ni_{10}Pd_1$ from 1.395 V to 1.670 V. (H) OER schematic mechanism and equivalent circuit models of $Ni_{10}Pd_1$ nanoplates in 1 mol/L KOH.

Electrochemical impedance spectroscopy (EIS) was carried out to evaluate the electrocatalytic kinetics of Ni-noble metal nanoplates for OER (Fig. 3F). The charge-transfer resistance (R_{ct}) was determined from the distinctive semicircle registered at low frequencies (high Z'), exhibiting a discernible order in the R_{ct} of $Ni_{10}Pd_1$ < $Ni_{10}Au_1$ < $Ni_{10}Ag_1$. The variational tendency of the R_{ct} was consistent with LSV results. The smaller R_{ct} of $Ni_{10}Pd_1$ nanoplates imparted faster electrode kinetics. To unravel the interface electron transfer reactions, EIS Nyquist and Bode plots and during OER for $Ni_{10}Pd_1$ were displayed in Fig. S15 (Supporting information) and Fig. 3G, accompanied by the corresponding OER schematic mechanism and equivalent circuit models (Fig. 3H). $Ni_{10}Pd_1$ catalyst displayed negligible charge transfer at the high-frequency interface, signifying that the high-frequency interface was exclusive to the original electrocatalyst oxidation without the involvement of OER. The OER occurred at the low-frequency interfaces when the applied potential was higher than 1.495 V, performed with the drastic decrease of phase angle at the low-frequency interface. According to the energy band theory, d electronic holes have a positive effect on the catalytic reaction, with a cardinal principle that an augmented abundance of d electronic holes corresponds to an amplified catalytic activity. Notably, Pd, Au and Ag exhibit the valence electron configurations of $4d^{10}5s^0$, $5d^{10}6s^1$ and $4d^{10}5s^1$, respectively. While the d electron orbitals of Pd, Au and Ag are full state, Pd uniquely possesses an empty 5s orbit, rendering its 4d electrons more prone to transition and forming a vacant d electron orbit. Additionally, the porous defects of the Ni metal substrate imparted a strategic advantage by increasing the active dot density of the Pd catalyst and constraining Pd cluster size. The symbiotic interplay between the porous structure and smaller Pd clusters contributes to improve the specific surface area of the catalyst, thereby enhancing the chemical adsorption of the material and achieving the best catalytic activity [37-39].

A series of Ni-Pd catalysts with Ni:Pd ratios of 2:1, 1:1, and 1:2 (denoted as Ni_2Pd_1, Ni_1Pd_1, and Ni_1Pd_2, respectively) were further synthesized for the composition optimization. The varying Ni:Pd ratios help to systematically investigate the size effect of Pd

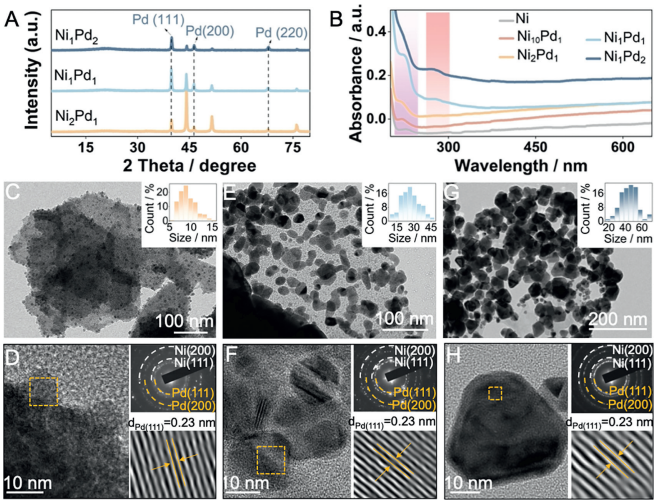

Fig. 4. Compositional and structural characterizations on Ni-Pd catalysts with different Ni/Pd compositions. (A) XRD patterns and (B) UV–vis spectra. TEM image of (C) Ni_2Pd_1, (E) Ni_1Pd_1 and (G) Ni_1Pd_2. The insets show the corresponding Pd particle size distribution. HRTEM and corresponding inverse FFT and SAED of (D) Ni_2Pd_1, (F) Ni_1Pd_1 and (H) Ni_1Pd_2.

clusters concerning Pd oxidation, atomic utilization, and catalytic performances. The composition and crystallographic structures of these Ni-Pd catalysts were characterized by XRD (Fig. 4A). Gradually pronounced diffraction peaks of Pd (111), (200), and (220) were observed with increasing Pd concentration, indicating the generation of metallic Pd after the displacement reaction. The similar trend of enhanced absorption peak for Pd is also reflected at ~280 nm in the ultraviolet-visible (UV–vis) spectroscopy (Fig. 4B). No significant differences in the basic nanoplate morphology were observed for the Ni-Pd catalysts (Fig. S16 in Supporting information). The proportion of the incorporated Pd element determined by corresponding EDS was nearly equivalent to the inputs of raw materials, indicating that the partial Ni substrate has been successfully substituted by Pd element (Figs. S17-S19 in Supporting information).

TEM images of Ni_2Pd_1, Ni_1Pd_1, and Ni_1Pd_2 nanoplates validated the uniform distribution of Pd clusters of varying sizes on Ni support (Figs. 4C, E and G). The size distribution of Pd clusters on $Ni_{10}Pd_1$, Ni_2Pd_1, Ni_1Pd_1 and Ni_1Pd_2 nanoplates revealed an increasing trend of Pd cluster size along with the increasing Pd concentration. Specifically, the average size of Pd clusters on $Ni_{10}Pd_1$, Ni_2Pd_1, Ni_1Pd_1, and Ni_1Pd_2 catalysts are approximately 5.57 nm, 9.27 nm, 26.85 nm, and 44.44 nm, respectively (the insets in Figs. 4C, E and G). The corresponding elemental mapping of Ni_2Pd_1, Ni_1Pd_1 and Ni_1Pd_2 nanoplates allow for a direct discrimination of the element of Pd and Ni, affirming the successful dopant of Pd element (Figs. S20-S22 in Supporting information). Similarly, an interplanar distance of 0.23 nm was detected in all HRTEM and inverse FFT images of Ni_2Pd_1, Ni_1Pd_1, and Ni_1Pd_2 catalysts, corresponding to the Pd (111) lattices. The corresponding SAED patterns simultaneously show the diffraction rings of Ni and Pd (Figs. 4D, F and H).

X-ray photoelectron spectroscopy (XPS) was employed to meticulously analyze the surface composition and valence state of Pd and Ni elements in the Ni-Pd catalysts. As shown in Fig. 5A, the Pd 3d spectra render to Pd $3d_{5/2}$ and Pd $3d_{3/2}$. After fitting, Pd^0 species were identified at 335.86 eV and 341.18 eV, and Pd^{2+} species were located at 337.36 eV and 342.56 eV, respectively. Different from $Ni_{10}Pd_1$ in which only Pd^0 species were detected, the peaks of Pd^{2+} species gradually intensified in Ni_2Pd_1, Ni_1Pd_1, and Ni_1Pd_2 catalysts, which confirmed that Pd concentration strongly correlated with an augmented Pd cluster size, resulting in extremely pronounced surface oxidation of Pd. The Ni 2p spectra also illustrated that the Ni species in Ni-Pd catalysts predominantly manifest as Ni^{2+} with the signal locating at 856.22 eV and 874.21 eV accompanied by satellite peaks at 861.78 eV and 880.07 eV, respectively (Fig. 5B). The faint peak of Ni^0 gradually diminished in $Ni_{10}Pd_1$, Ni_2Pd_1, and Ni_1Pd_1, suggesting that the increased Pd concentration also exacerbated the surface oxidation of Ni. The severe surface oxidation of Ni to Ni^{2+} might constitute a crucial reason for the low intrinsic catalytic activity of the individual Ni catalyst.

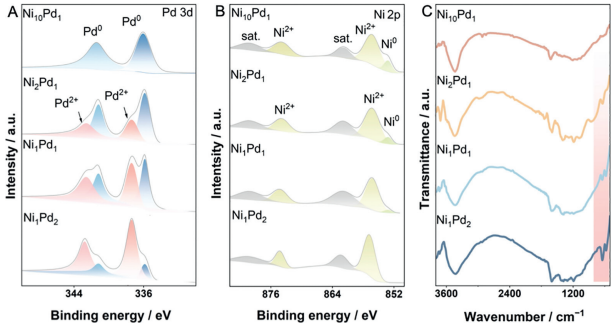

Fig. 5. XPS spectra of (A) Pd 3d and (B) Ni 2p. (C) FTIR spectra of Ni-Pd catalysts.

The surface oxidation was also reflected in Fourier transforms infrared spectroscopy (FTIR), as shown in Fig. 5C. The broad adsorption band at around 3400 cm^{-1} was attributed to O–H groups. Additionally, the absorption band at the range of 650–570 cm^{-1} was related to M-O bonds, where M could be Ni or Pd. The intense trend of M-O bonds was $Ni_{10}Pd_1$ < Ni_2Pd_1 < Ni_1Pd_1 < Ni_1Pd_2, which suggested that the increased Pd concentration led to the changes in the chemical structure of composites, intensifying surface oxidation through generating M-O bonds. Thus, the augmentation of Pd concentration held the potential to increase reactive sites for noble metal, yet the concomitant increase in Pd cluster size. The increment in Pd cluster size concurrently raised the facile surface oxidation, resulting in a significant compromise in OER activity.

To estimate the effects of Pd clusters particle size and surface oxidation on electrocatalytic performance, OER and MOR electrochemical measurements were conducted in a standard three-electrode system (Fig. 6). The Pd concentration rendered no significant effect on the specific OER activity for the Ni-Pd catalysts (Fig. 6A and Fig. S23 in Supporting information). However, the best-performing $Ni_{10}Pd_1$ showed up as the high mass-specific OER activity of 0.085 A/mg_{Pd} at 1.5 V (normalized by Pd loading mass), displaying more than 3.86-, 7.08-, and 6.54-fold enhancement compared to Ni_2Pd_1, Ni_1Pd_1, and Ni_1Pd_2, respectively (Fig. 6B). The higher mass activity confirmed that the small size of Pd clusters contributed to the alleviated surface oxidation, thereby effectively maximizing the reactivity and the atomic efficiency of noble metals. EIS also showed a similar trend of the sluggish OER kinetics for Ni-Pd nanoplates along with the increased Pd concentration (Fig. 6C).

The MOR performance of Ni-Pd catalysts was evaluated by CV in Ar-purged 1.0 mol/L KOH and 1.0 mol/L CH_3OH electrolyte solution. Despite the Ni_1Pd_2 catalyst displaying the higher specific activity than $Ni_{10}Pd_1$, Ni_2Pd_1 and Ni_1Pd_1 (Fig. 6D), the mass electroactivity of $Ni_{10}Pd_1$ was superior to those of the congeneric Ni-Pd catalysts (Fig. 6E). The forward peak mass current densities (I_f) for Ni-Pd catalysts were 0.401, 0.105, 0.110, and 0.092 A/mg_{Pd}, respectively (Fig. 6F). Generally, a higher ratio of the forward peak mass current density to backward peak mass current density (I_f/I_b) indicated the superior resistance to the poisoning of carbonaceous

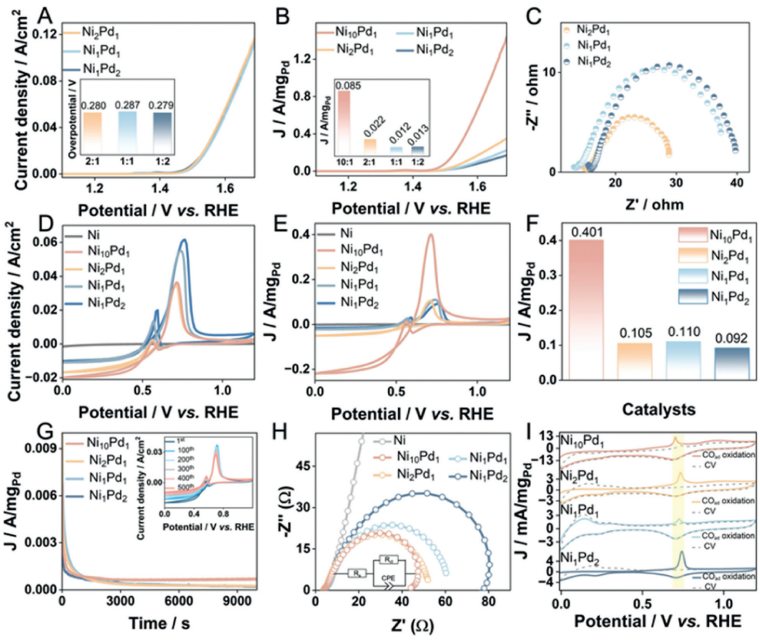

Fig. 6. OER and MOR performance of Ni-Pd nanocomposites with different Ni/Pd ratios. (A) IR-corrected LSV curves, (B) mass activity and (C) Nyquist plots toward OER. (D) The specific current density and (E) mass activity obtained in the mixed electrolyte of 1.0 mol/L KOH and 1.0 mol/L CH_3OH. (F) The comparison of mass activities recorded at I_f peak current. (G) Chronoamperometry curves, the inset is multi-cycled CV curves of $Ni_{10}Pd_1$ catalyst. (H) Nyquist plots and (I) CO-stripping voltammograms for as-prepared Ni-Pd catalysts.

species. Herein, the $Ni_{10}Pd_1$, Ni_2Pd_1, Ni_1Pd_1, Ni_1Pd_2 exhibited I_f/I_b values of 26.7, 15, 4.1, 3.1, respectively, indicating that $Ni_{10}Pd_1$ enhanced MOR electrocatalytic activity. The $Ni_{10}Pd_1$ exhibited the highest mass electroactivity, signifying the pivotal role of Pd content in MOR electroactivity enhancement.

Besides the catalytic activity, the stability of catalysts was assessed by chronoamperometry (Fig. 6G). The mass current density of $Ni_{10}Pd_1$ catalyst exhibited a rapid drop initially and a slight decrease at the subsequent times, outperforming those of Ni_2Pd_1, Ni_1Pd_1, and Ni_1Pd_2. Additionally, the long-term stability was also evidenced by multi-cycled CV curves recorded at 50 mV/s. The forward peak mass current density of $Ni_{10}Pd_1$ catalyst exhibited only a slight decrease after 500 cycles, indicating a better stability compared to Ni_2Pd_1, Ni_1Pd_1, and Ni_1Pd_2 (Figs. S24-S26 in Supporting information). Furthermore, the $Ni_{10}Pd_1$ catalyst delivered faster charge transfer than Ni_2Pd_1, Ni_1Pd_1 and Ni_1Pd_2, which effectively reflected the intrinsic electroactivity of electrocatalysts (Fig. 6H). The anti-poisoning ability was demonstrated by CO-stripping measurements in 1.0 mol/L KOH solution (Fig. 6I). Notably, the peak potential of CO electro-oxidation of $Ni_{10}Pd_1$ (0.702 V) was much more negative than those of Ni_2Pd_1 (0.734 V), Ni_1Pd_1 (0.726 V), and Ni_1Pd_2 (0.743 V), revealing that $Ni_{10}Pd_1$ not only exhibited the improved electroactivity for MOR but also demonstrated an enhanced anti-poisoning ability. Hence, it was concluded that the size of Pd clusters anchored on Ni substrate significantly influenced the oxidation states of Pd and Ni surfaces by altering the chemical structure of the catalyst. The above experimental findings elucidated that the smaller Pd clusters were more effective in activating more active sites accessible, enhancing the Pd atomic utilization. As a result, $Ni_{10}Pd_1$ exhibits the optimal performance.

In summary, a facile approach was developed for the preparation of Ni-noble metal (Pd, Au and/or Ag) nanoplates *via* partially replacing Ni in Ni-Al LDH precursor. Among a series of Ni-noble metal nanocatalysts, $Ni_{10}Pd_1$ exhibited superior OER electrocatalytic properties. Moreover, the effects of Pd cluster size, atomic utilization, and surface oxidation on OER and MOR electrocatalytic performances were systematically investigated on Ni-Pd nanoplates with different Ni/Pd ratios. The porous nanoarchitecture of Ni metal substrate was beneficial to uniformly anchor Pd clusters, avoiding agglomeration and thus controlling the cluster size. The synergistic combination of porous Ni metal substrate with trace Pd not only can effectively reduce the Pd loading mass to improve Pd atomic utilization, but also modify the electronic state of Pd atoms to facilitate the transmission of active species and anti-poisoning ability. As a result, $Ni_{10}Pd_1$ catalyst with an average Pd size of 5.6 nm demonstrated higher mass activity than all Ni_2Pd_1, Ni_1Pd_1 and Ni_1Pd_2 toward alkaline OER and MOR. This work introduces a novel strategy for designing high-activity transition metal-noble metal electrocatalysts through controlled loading clusters for diverse electrocatalytic reactions.

Declaration of competing interest

The authors declare that they have no known competing financial interests or personal relationships that could have appeared to influence the work reported in this paper.

CRediT authorship contribution statement

Fenglin Wang: Conceptualization, Formal analysis, Investigation, Methodology. **Chengwei Kuang:** Data curation, Formal analysis. **Zhicheng Zheng:** Formal analysis, Investigation. **Dan Wu:** Resources, Software. **Hao Wan:** Formal analysis, Project administration, Writing – review & editing. **Gen Chen:** Project administration, Supervision, Writing – review & editing. **Ning Zhang:** Resources, Validation. **Xiaohe Liu:** Funding acquisition, Supervision. **Renzhi Ma:** Conceptualization, Supervision.

Acknowledgments

The authors acknowledge the financial support by the National Natural Science Foundation of China (Nos. U20A20123, 51874357, 22379166), Natural Science Foundation for Distinguished Young Scholars of Hunan Province (No. 2022JJ10089).

Supplementary materials

Supplementary material associated with this article can be found, in the online version, at doi:10.1016/j.cclet.2024.109989.

References

[1] Z. Wen, W. Fang, F. Wang, et al., Angew. Chem. Int. Ed. 63 (2024) e202314876.
[2] Y. Liang, Y. Li, H. Wang, et al., J. Am. Chem. Soc. 135 (2013) 2013–2036.
[3] H. Wan, R. Ma, X. Liu, et al., ACS Energy Lett. 3 (2018) 1254–1260.
[4] J. Mei, Y. Deng, X. Cheng, et al., Chin. Chem. Lett. (2023) 108900.
[5] W. Fang, Z. Wen, F. Wang, et al., Sci. Bull. 69 (2024) 1686–1696.
[6] W. Ma, R. Ma, J. Wu, et al., Nanoscale 8 (2016) 10425–10432.
[7] Y. Jiao, Y. Zheng, M. Jaroniec, et al., Chem. Soc. Rev. 44 (2015) 2060–2086.
[8] M. Gong, H. Dai, Nano Res. 8 (2014) 23–39.
[9] J. Li, Y. Yu, S. Xu, et al., Acta Phys. Chim. Sin. 39 (2023) 2302049.
[10] A.T. Swesi, J. Masud, M. Nath, Energy Environ. Sci. 9 (2016) 1771–1782.
[11] C.X. Guo, S. Chen, X. Lu, Nanoscale 6 (2014) 10896–10901.
[12] C. Wang, Y. Sui, M. Xu, et al., ACS Sustain. Chem. Eng. 5 (2017) 9787–9792.
[13] Z.X. Lu, Y. Shi, C.F. Yan, et al., Int. J. Hydrogen Energy 42 (2017) 3572–3578.
[14] L. Wei, H.E. Karahan, S. Zhai, et al., Adv. Mater. 29 (2017) 1701410.
[15] Y. Lee, J. Suntivich, K.J. May, et al., J. Phys. Chem. Lett. 3 (2012) 399–404.
[16] N.T. Suen, S.F. Hung, Q. Quan, et al., Chem. Soc. Rev. 46 (2017) 337–365.
[17] O. Diaz-Morales, I. Ledezma-Yanez, M.T.M. Koper, et al., ACS Catal. 5 (2015) 5380–5387.
[18] Q. Wu, R. Zhou, Z. Yao, et al., Chin. Chem. Lett. 35 (2024) 109416.
[19] X. Zhang, H. Xu, X. Li, et al., ACS Catal. 6 (2015) 580–588.
[20] H. Mei, W. Wu, B. Yu, et al., Sensor. Actuat. B: Chem. 223 (2016) 68–75.
[21] R. Kavian, S.I. Choi, J. Park, et al., J. Mater. Chem. A 4 (2016) 12392–12397.
[22] B.M. Tackett, W. Sheng, S. Kattel, et al., ACS Catal. 8 (2018) 2615–2621.
[23] F. Wang, Z. Wen, Z. Zheng, et al., Adv. Energy Mater. 13 (2023) 2203830.
[24] M.S. Faber, S. Jin, Energy Environ. Sci. 7 (2014) 3519–3542.
[25] C. Yang, O. Fontaine, J.M. Tarascon, et al., Angew. Chem. Int. Ed. 56 (2017) 8652–8656.
[26] J. Li, Z. Xi, Y.T. Pan, et al., J. Am. Chem. Soc. 140 (2018) 2926–2932.
[27] Z. Zhao, H. Liu, W. Gao, et al., J. Am. Chem. Soc. 140 (2018) 9046–9050.
[28] J. Li, S. Sharma, X. Liu, et al., Joule 3 (2019) 124–135.
[29] X. Wang, S.I. Choi, L.T. Roling, et al., Nat. Commun. 6 (2015) 7594.
[30] C. Li, X. Chen, L. Zhang, et al., Angew. Chem. 133 (2021) 7753–7758.
[31] D. Du, Q. Geng, L. Ma, et al., Chem. Sci. 13 (2022) 3819–3825.
[32] H. Wang, S. Liu, H. Zhang, et al., New J. Chem. 44 (2020) 15492–15497.
[33] Y.X. Xiao, J. Ying, G. Tian, et al., Chem. Commun. 57 (2021) 986–989.
[34] H.H. Li, S.Y. Ma, Q.Q. Fu, et al., J. Am. Chem. Soc. 137 (2015) 7862–7868.
[35] D.A. Cantane, F.E.R. Oliveira, S.F. Santos, et al., Appl. Catal. B: Environ. 136-137 (2013) 351–360.
[36] F. Wang, G. Chen, X. Liu, et al., ACS Sustain. Chem. Eng. 7 (2018) 341–349.
[37] L. Zhang, Q. Chang, H. Chen, et al., Nano Energy 29 (2016) 198–219.
[38] L. Sun, B. Liao, X. Ren, et al., Electrochim. Acta 235 (2017) 543–552.
[39] G.K. Wertheim, S.B. DiCenzo, D.N. Buchanan, Phys. Rev. B 33 (1986) 5384–5390.